Journal of Advanced Research 30 (2021) 75–84

Contents lists available at ScienceDirect

Journal of Advanced Research

journal homepage: www.elsevier.com/locate/jare

Robotic *in situ* 3D bio-printing technology for repairing large segmental bone defects

Lan Li [a,b,e,1], Jianping Shi [a,c,1], Kaiwei Ma [b], Jing Jin [a], Peng Wang [a,e], Huixin Liang [a,e], Yi Cao [d,*], Xingsong Wang [b,*], Qing Jiang [a,e,*]

[a] State Key Laboratory of Pharmaceutical Biotechnology, Department of Sports Medicine and Adult Reconstructive Surgery, Drum Tower Hospital Affiliated to Medical School of Nanjing University, China
[b] School of Mechanical Engineering, Southeast University, China
[c] School of Electrical and Automation Engineering, Nanjing Normal University, China
[d] National Laboratory of Solid State Microstructures, Department of Physics, Nanjing University, China
[e] Jiangsu Engineering Research Center for 3D Bioprinting, China

GRAPHICAL ABSTRACT

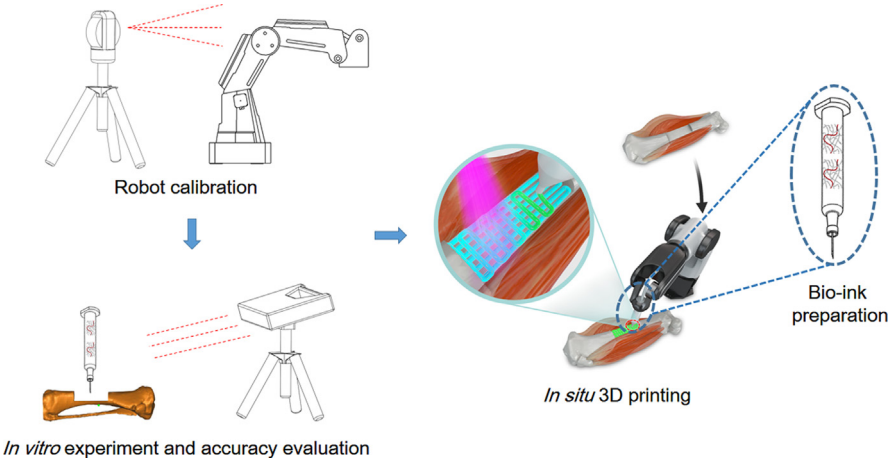

ARTICLE INFO

Article history:
Received 10 March 2020
Revised 14 October 2020
Accepted 24 November 2020
Available online 25 November 2020

Keywords:
3D bio-printing

ABSTRACT

Introduction: The traditional clinical treatment of long segmental bone defects usually requires multiple operations and depends on donor availability. The 3D bio-printing technology constitutes a great potential therapeutic tool for such an injury. However, *in situ* 3D bio-printing remains a major challenge.
Objectives: In this study, we report the repair of long segmental bone defects by *in situ* 3D bio-printing using a robotic manipulator 3D printer in a swine model.
Methods: We systematically optimized bio-ink gelation under physiological conditions to achieve desirable mechanical properties suitable for bone regeneration, and a D-H kinematic model was used to improve printing accuracy to 0.5 mm.

Peer review under responsibility of Cairo University.

* Corresponding authors at: National Laboratory of Solid State Microstructures, Department of Physics, Nanjing University, No.22 Hankou Road, Nanjing 210000, China (Y. Cao). School of Mechanical Engineering, Southeast University, No.2 Southeast University Road, Nanjing, 210000, China (X. Wang). State Key Laboratory of Pharmaceutical Biotechnology, Department of Sports Medicine and Adult Reconstructive Surgery, Drum Tower Hospital affiliated to Medical School of Nanjing University, Nanjing University, No. 321 Zhongshan Road, Nanjing 210000, China (Q. Jiang).
E-mail addresses: caoyi@nju.edu.cn (Y. Cao), xswang@seu.edu.cn (X. Wang), qingj@nju.edu.cn (Q. Jiang).
[1] Lan Li and Jianping Shi contributed equally to this work.

https://doi.org/10.1016/j.jare.2020.11.011

In situ
Regenerative medicine
Robotic
Tissue engineering

Results: These technical improvements allowed the repair of long segmental defects generated on the right tibia of pigs using 3D bio-printing within 12 min. The 3D bio-printing group showed improved treatment effects after 3 months.
Conclusion: These findings indicated that robotic *in situ* 3D bio-printing is promising for direct clinical application.

Introduction

Large segmental defects are generally reflected by critical bone damage, generally with a circumferential loss exceeding 50% or a length above 2 cm in adult patients [1]. Traditional therapeutic modalities for these defects using autogenous or allogeneic bone grafts [2] are hampered by multiple hurdles, including donor site morbidity, limited volume availability, graft incorporation and remodeling, no structural capability or osteogenic properties, and potential disease transmission [3,4]. The three dimensional (3D) bio-printing technology may provide new solutions to this tremendous clinical challenge.

The three dimensional bio-printing technology is considered an effective tool in regenerative medicine, initiating a grand revolution in traditional tissue engineering (TE). With the help of computer-aided design (CAD) and computer-aided manufacturing (CAM), the 3D bio-printing technology precisely places cells and biological materials in predefined locations to produce TE scaffolds [5]. Various additive production methods, including inkjet printing, bio-extrusion, laser-based printing, and photopolymerization, are available for scaffold generation *in vitro* [6–8]. The current strategy for 3D bio-printing is to culture cells in a scaffold generated by introducing materials using the additive manufacturing technology and modulating agents for creating a mature tissue *in vitro* before implantation [9–11]. Various tissues and organs, including the heart valve, cartilage, bone myocardial tissue, trachea, and blood vessels, have been restored in this manner [12,13]. This method generally requires several weeks to complete the whole process before scaffold implantation *in vivo*, which hampers the clinical application of 3D bio-printing.

The emergence of *in situ* 3D bio-printing has revolutionized the field. A few studies have assessed *in situ* 3D bio-printing for clinical use or injury repair, and demonstrated that this method could be used to restore bone defects [14–16]. Due to the special microenvironment, including large amounts of autologous mesenchymal stem cells and the superficial injury site, repairing bone and cartilage damage by direct 3D bio-printing is considered a promising entry point for applying the novel tissue engineering technology in clinic. By 3D scanning, the shape of the damaged area can be easily assessed; then, the shape of the 3D printing object is determined with a reverse engineering software (e.g., Magics software) in a few minutes. This technology makes it possible to repair defects with complex shapes in a short time.

In this work, we explored the feasibility of repairing large segmental bone defects in large living animal models by the *in situ* 3D bio-printing technology. In a previous study, we reported the possibility of fixing segmental bone defects of the humerus in small animal models (New Zealand rabbits) *in vitro* with a bio-ink containing sodium alginate and polyethylene glycol diacrylate (PEGDA) [14]. These bone defects could be precisely filled with the bio-ink using a modified 3D printer, with the shapes of scaffolds maintained by the photopolymerization reaction. We also demonstrated the feasibility of using the industrial 6-DOF robot 3D printer in *in situ* cartilage regeneration in small animal models [17]. Here, this technique was further improved for direct *in situ* 3D printing in large living animal models for injury repair. To this end, several steps were employed, including bio-ink synthesis and characterization, robotic calibration and printing path planning, the establishment of a large bone defect model in swine, and *in situ* 3D bio-printing and its evaluation for osteogenesis ability. We anticipate that these technical advances could serve as the cornerstone of the clinic application of *in situ* 3D bio-printing for repairing large segmental bone defects.

Materials and methods

The study followed relevant guidelines, and had approval from the ethics committee of Drum Tower Hospital affiliated to the Medical School of Nanjing University.

Materials

Sodium alginate (medium viscosity), PEGDA (700 kDa), 2-hydroxy-4′-(2-hydroxyethoxy)-2-methylpropiophenone (Irgacure™ 2959, or I-2959), N,N-methylene-bis(acrylamide) (MBA), $CaCl_2$, NaOH, gelatin (gel strength ~300 g Bloom), methacrylic anhydride (MA), and ALP kit were provided by Sigma Aldrich. Dulbecco's phosphate buffered saline (DPBS) was provided by Gibco.

Methacrylated gelatin synthesis

GelMA synthesis was carried out as reported previously [18]. In brief, type A gelatin was dissolved in DPBS with stirring at 60 °C to a final concentration of 10% (w/v). Then, MA was added dropwise at 0.5 ml/min for a 3-h incubation at 50 °C. The solution was then transferred into tubes, and unreacted MA was removed by centrifugation at 3500*g* for 3 min. The resulting supernatant was diluted with two volumes of Ultra-Pure water and dialyzed for 5–7 days using a dialysis membrane with a 12-kDa molecular weight cut off (MWCO). The pH of the dialyzed GelMA solution was adjusted to 7.4 with 1 M $NaHCO_3$, followed by lyophilization until complete GelMA dehydration.

Bio-ink preparation

The components of the bio-ink were sterilized by UV light, and the preparation process was performed in a aseptic environment based on a previous study [14]. A solution of 6% (w/v) sodium alginate and 80 mM $CaCl_2$ were mixed in equal volumes to yield a partially cross-linked hydrogel [19]. This was followed by addition of 10% (w/v) PEGDA, 5% (w/v) GelMA, and 0.05% (w/v) I-2959 for generating photoinitiating conditions compatible to cells.

Characterization of the bio-ink

Uncross-linked bio-ink with different filament diameters were transferred to a Haake Mars 40 rheometer plate (Thermo Scientific) to determine crosslinking times under different ultraviolet (UV) intensities. The pre-fabricated samples using a mold with a height of 10 mm and a diameter of 8 mm were employed in the compression test. Compression stress-strain tests were performed on an

Instron-5944 universal instrument equipped with a 2 kN sensor. In the loading–unloading cycle assay, the compression rate was maintained at 4% s^{-1} based on the original height of the hydrogel, roughly 16–24 mm/min. In the compression-crack test, the rate of compression was 2% s^{-1} with respect to the original height of the hydrogel, roughly in the range of 8–12 mm/min. The toughness E_f was calculated from the area below the compression stress-strain curve until fracture by the following equation: $E_f = \int_{x_0}^{x_f} \sigma(x)dx$, where σ is the stress, and x_0 and x_f represent the starting and fracture strains of the compression, respectively. The Young's modulus comprised approximate linear fitting values under 10–20% strain deformation. Triplicate measurements were performed of multiple bio-ink samples.

Biocompatibility evaluation of the bio-ink

Bio-ink samples were fabricated using mold with a height of 1 mm and a diameter of 8 mm were used in this test. MC3T3-E1 cells, a cell line derived from mice embryonic osteoblast precursor cells, were employed to evaluate the biocompatibility of the bio-ink. Briefly, the cells were seeded on the cross-linked bio-ink in the osteogenic induction medium with 50 μg/ml ascorbic acid and 10 mM sodium β-glycerophosphate. Phalloidin/DAPI staining was performed after seeding for 4 h, 1 day, and 3 days to observe cell morphology. Quantitative real-time PCR was performed at day 7 and 14 to evaluate cell differentiation markers. Four typical genes were measured on a 7300 Real-Time PCR System (Applied Biosystems, MA, USA) with SYBR Premix Ex Taq. Forward and reverse primers are shown in Table S1. GAPDH was employed for the normalization of triplicate assays. The cells cultured on blank dishes constituted the control group. Alkaline Phosphatase (ALP) activity measurement was performed at day 7 and 21. Briefly, the samples were cut into pieces with scissors after 7 or 21 days of co-culture. These pieces were sonicated and centrifuged, and mixed with substrate solution (SIGMA FASTTM p-nitrophenyl phosphate and Tris buffer tablets, Sigma). Absorbance at 405 nm was detected to evaluate ALP activity.

In vitro experiments

After the error model and the kinematic model of the robot were established (Figs. S1A, Table S2), the *in vitro in situ* 3D printing tests before and after error compensation were performed on the isolated tibia. The printing accuracy was measured with the Geomagic Control software (Geomagic, USA) according to a previous study [14]. Briefly, the healthy isolated tibia was scanned with a GE Lightspeed 16 CT instrument (slice distance, 0.625 mm; field of view [FOV], 500 mm). The generated images underwent conversion into DICOM files for 3D reconstruction with the MIMICS 19.0 software (Materialise, Leuven, Belgium). After the defect was created and the *in situ* 3D printing process was completed, bone scanning was performed with a 3D handheld scanner (EinScan-Pro, Shining 3D, China). The high-definition mode was selected for scanning. The digital models were imported into the Geomagic Control software, and a 3D Comparison operation was performed in the software to measure printing accuracy.

3D printing path planning

The printing model with a length of 30 mm, widths of 16 mm and 14 mm at the proximal and distal ends, respectively, and a depth of 7 mm was generated with Magics 21.0 (Materialise, Belgium) before surgical operation through a virtual surgery using a customized guide plate. The geometry of the printed scaffold is depicted in Fig. S1B. The 3D printing path was planned with an open source slicing software (Repetier Host). The printing speed was 6 mm/s, while the separation distance between two filaments was 1.2 mm according to our previous study [20]. The thickness of the model was set to 300 μm, with a filling angle θ of 0° or 90° in the software (Fig. S1C). The G-code file was imported in the operation system of the robot for future direct printing.

Establishment of large segmental bone defects in swine

All animal experiments (including euthanasia with lidocaine and propofol) were performed according to the regulations of the ethics committee of Drum Tower Hospital affiliated to the Medical School of Nanjing University, following the ARRIVE and IACUC guidelines. The ethical committee number for the present study was *2019AE05002*.

Six male Bama mini pigs (25 kg) were assessed, in an environment at 22 ± 1 °C with 50 ± 1% relative humidity under a 12–12 h light/dark cycle. The pigs were divided into two groups, including the blank control and 3DP groups, respectively. Upon anesthesia, the right tibia was completely exposed via a lateral incision. A bone defect was generated at the middle segment of the tibia according to the guide plate.

In situ 3D bio-printing

The robot was placed near the surgical area, and an extrusion-based 3D printing nozzle with a diameter of 400 μm was immobilized at the end of the robotic arm. Air pressure was set at 0.3 MPa during the 3D printing process. Hydrogel was printed and photopolymerized with a UV lamp at an intensity of 100 mW/cm^2, for each layer for repairing the defects. This light intensity has little impact on cell viability and live subjects [21]. In the 3DP group, bone defects were treated by the direct 3D bio-printing operation, with internal fixation by a titanium plate utilized to maintain tibial strength. In the blank control group, no implants were filled in the defects, but the same internal fixation method was employed. Cefuroxime sodium was administered intramuscularly for 3 days post-operation to prevent infection. All animals were sacrificed 12 weeks postoperatively, to assess new bone formation.

Computed tomography measurement and histological analysis

Tibial bones were harvested and scanned on a VivaCT-80 micro-CT system (Scanco Medical, Brüttisellen, Switzerland) at 70 kV and 145μA, with a field of view (FOV) of 63.9 mm and a nominal isotropic image voxel size of 62.4 μm. The bone volume to total volume (BV/TV) ratio, trabecular number (Tb.N), trabecular thickness (Tb.Th), and trabecular separation (Tb.Sp) were analyzed using the micro-CT system. The acquired images were converted into DICOM files for subsequent analysis. The 3D reconstruction of scaffolds and the newly formed bones was performed with the MIMICS 19.0 software. The same threshold value was used for 3D reconstruction.

After CT examination, the samples underwent fixation in formalin at 4 °C overnight, rinsing with distilled water, dehydration with graded alcohol, and embedding in polymethyl methacrylate (PMMA) with no decalcification. The specimens were then sectioned at 30 μm with a diamond-coated saw (310 CP; EXAKT, Germany), submitted to hematoxylin-eosin (H&E) and Goldner trichrome staining, and assessed by fluorescence microscopy (Olympus Corp., Tokyo, Japan). A modified scoring system according to Han et al. was used for semi-quantitative histological scoring [22]. The scoring criteria are listed in Table S3.

Statistical analysis

SPSS 19.0 (SPSS, USA) and IGOR Pro 6.12 (WaveMetrics, USA) were employed for data analysis. Data were evaluated by unpaired Student's *t*-test, and $P < 0.05$ indicated statistical significance.

Results

Gelation and mechanical features of the bio-ink

The photopolymerizable bio-ink was mainly composed of methacrylated gelatin (GelMA), sodium alginate, and polyethylene glycol diacrylate (PEGDA). GelMA deriving from partially hydrolyzed collagen from animal tissues could provide essential biochemical cues [23] and enhance the mechanical strength of the crosslinked bio-ink; both traits are essential for stimulating osteogenesis *in vitro* [14,24]. The loosely crosslinked alginate-calcium network was found to be important in maintaining the shape of the bio-ink before photopolymerization completion. The results of the rheological test are shown in **Figure S2**. The compositions, concentrations, and buffer conditions were first optimized. The resulting bio-ink quickly photopolymerized under physiological conditions (Fig. 1A). The photopolymerization reaction occurred within less than 10 s as the printing needle diameter was 400 μm and UV intensity was 150 mW/cm^2. The crosslinking time increased slightly with needle diameter but decreased dramatically after use of UV light of higher intensity. However, high UV intensity cannot be used in *in vivo* experiments due to potential damage to living tissues. The rapid gelation indicated that the bio-ink was suitable for *in situ* 3D bio-printing. The SEM images of the bio-ink and the 3D printed objects are depicted in Fig. S3.

In order to serve as a substrate for bone regeneration, high mechanical stability is also a prerequisite. In contrast to most fast gelation bio-inks that are rigid and fragile, our bio-ink showed outstanding mechanical stability. According to compression break test results (Fig. 1B), the Young's modulus of the bio-ink was 78.1 kPa, with a compression limit of 33.89%; the stress limit was 60.46 kPa, and a toughness of 71.35 kJ/m^3 was obtained. The stress-relaxation cycle with different strains (Fig. 1C) showed that energy dissipation increased from 54.72 J/m^3 to 449.18 J/m^3 with strain between 15% and 30% (Fig. 1D). The same variation trend was observed for the hysteresis between compression and relaxation. Uninterrupted compression-relaxation cycles to the same hydrogel (20 cycles with 30% strain and no time elapsed between cycles; Fig. 1E) demonstrated the recovery ability of the bio-ink under compression. The amount of energy dissipated was decreased to 60%, and the recovery rate remained above 90% after 20 cycles (Fig. 1F). The high toughness and recovery ability of the hydrogel made of the current bio-ink resulted from strong covalent and ionic crosslinking in the interpenetrating polymer networks.

The bio-ink also demonstrated remarkable biocompatibility. Obviously, cell attachment was observed 4 h after seeding, and higher cell density was found after 3 days of culture on the surface of the bio-ink (Fig. S4). The mRNA expression levels of osteogenic genes showed the same variation trend as the cell behavior. All mRNAs exhibited significant upregulation in the bio-ink group at day 7 and 14 (Fig. 2A). On day 7 and 21, ALP activity was significantly higher in the bio-ink group compared with the control group (Fig. 2B and C). These findings indicated that the biomechanical and biochemical properties of the bio-ink were suitable for bone tissue engineering.

3D printing accuracy

According to the coordinate error shown in Fig. S5, volatility curves in all axes were reduced after identification and compensation. Next, we quantitatively assessed printing accuracy after movement compensation. 3D comparison data are depicted in Fig. 3, with green indicating that both models could be entirely fitted. The results showed that the 3D error gradually increased with the color changing from green to red, and gradually decreased with the color changing to deep blue. We found that the main color of the printed region was red before identification and compensation (Fig. 3A). In addition, the pores were almost circular, indicating that the lack of standardization in the printing path and the printed volume did not result in filling of the defective region. However,

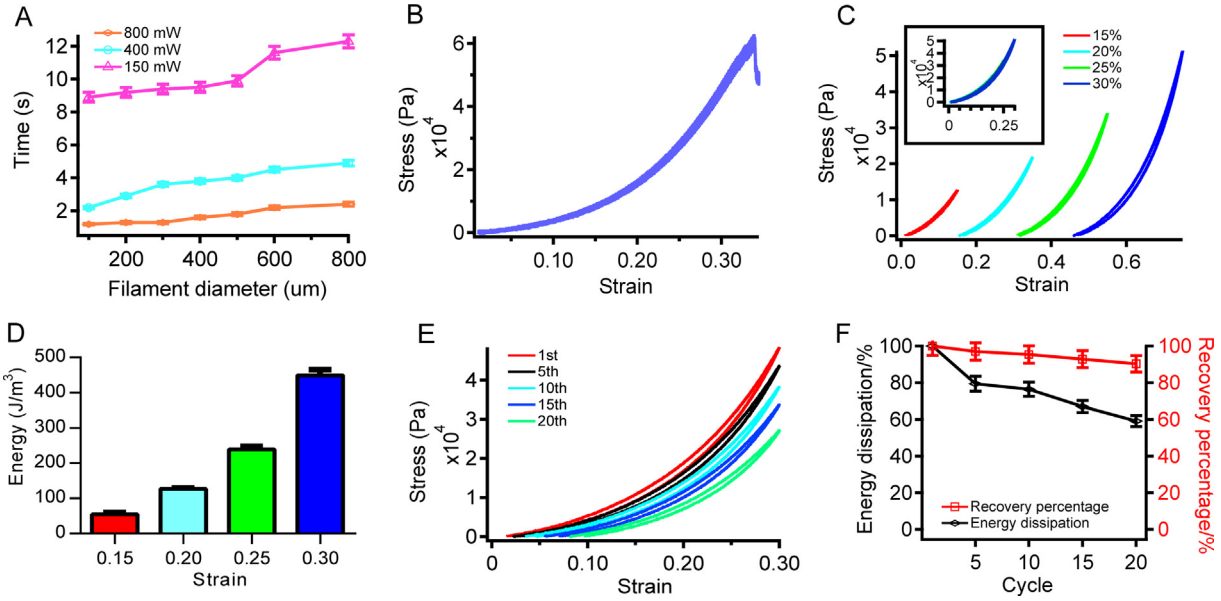

Fig. 1. Crosslinking time and compressibility of the bio-ink. (A) Crosslinking times of filaments with different diameters under different UV light intensities. (B) Compressibility of the bio-ink. (C) Stress–strain curves of the bio-ink. The compression strains in various cycles were 15%, 20%, 25%, and 30%, respectively. (D) Dissipated energy levels in various cycles. (E) Compression-relaxation cycles to the same specimen for 20 cycles with no interruption between consecutive cycles. The compression strain was set at 30%. (F) Dissipated energy (black) and recovery percentage (red) of the bio-ink.

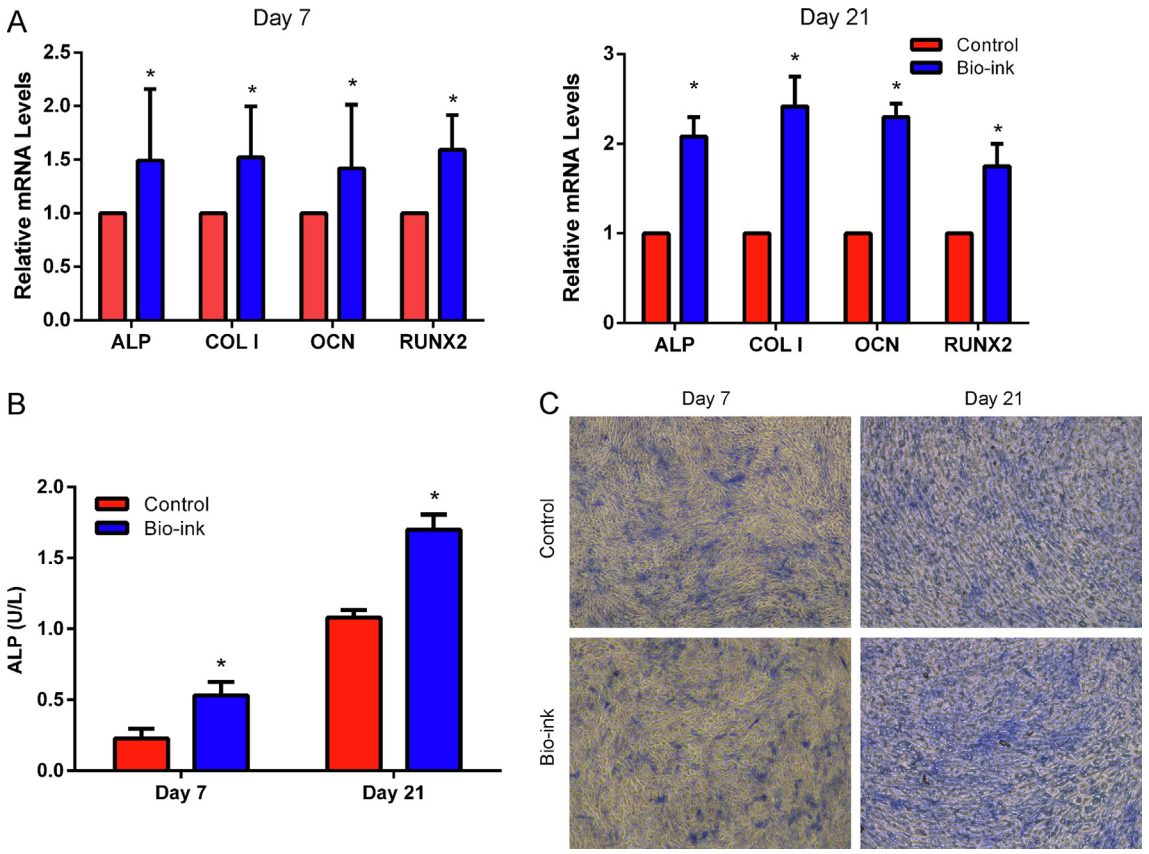

Fig. 2. Biocompatibility assessment of the bio-ink. (A) Gene expression levels at days 7 and 14. (B,C) ALP activity at day 7 and 21. *p < 0.05.

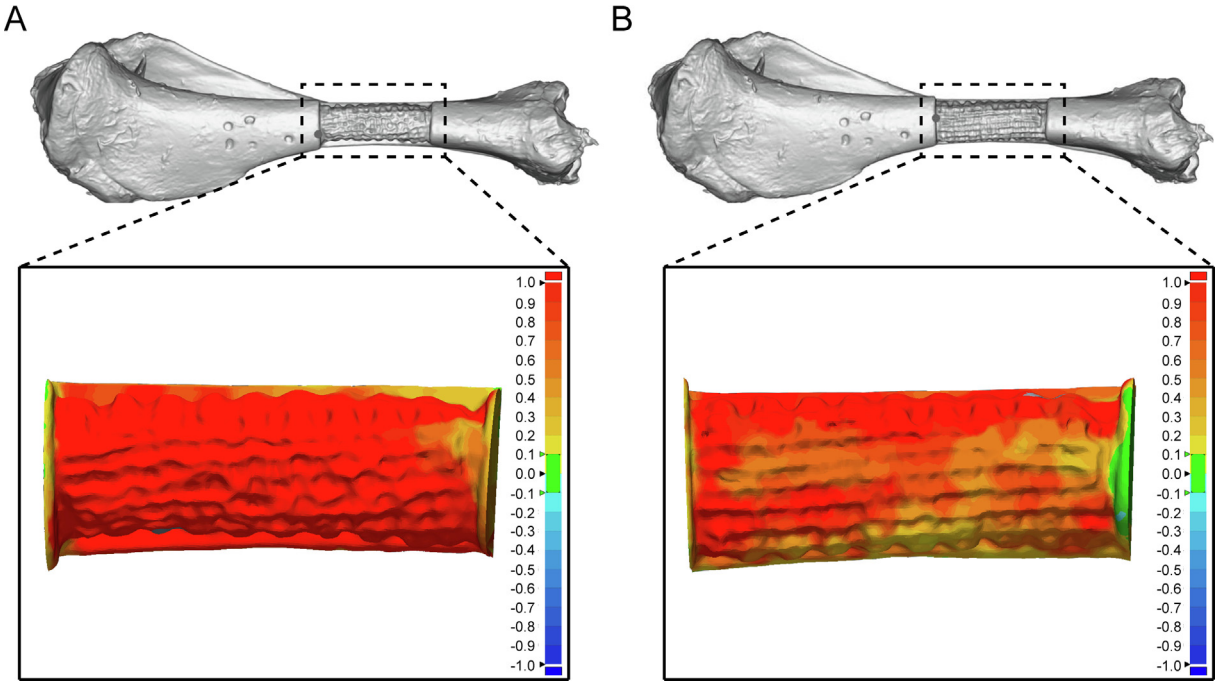

Fig. 3. In vitro printing test results. (A) 3D comparison between the 3D printed sample (before accuracy improvement) and the intact bone. (B) 3D comparison between the 3D printed sample (after accuracy improvement) and the intact bone.

the pores were square, with the main color transferred to red, orange, and light yellow (Fig. 3B), indicating that the printing path and the printed volume were improved after identification and compensation. The error interval was −0.1765 mm to 1.7857 mm before compensation, and decreased to −0.1430 mm to 1.7507 mm thereafter (Table S4). The mean error was also

decreased from 0.6964 ± 0.5771 mm to 0.5157 ± 0.4240 mm ($p < 0.05$). Volatility was reduced in the compensation group (dispersion degree, 0.3331 vs 0.1798), indicating the precise printing ability due to the identification and compensation operation. Additionally, the distribution of points was uniform in the workspace, and the maximum height and the longest distance reachable by the robot were 278.8038 mm and 337.8997 mm, respectively (Fig. S6).

In situ 3D bio-printing

Having rigorously optimized the bio-ink and the bio-printing robot, we next assessed direct *in situ* 3D bio-printing in living animals. A total of six pigs were enrolled in an *in vivo* study, and long segmental defects were generated on the right tibia. The whole process of *in situ* 3D bio-printing is shown in Fig. 4A. Because of UV light affecting the camera, video and photograph shootings during the demonstration process were performed away from light; photopolymerization was undertaken after the direct printing procedure. The robotic manipulator based 3D bio-printer was placed at the distal end of the hind leg, with the printing nozzle linked to the pneumatic control device (Fig. 4B). After defect generation, the nozzle was moved to the starting point of the printing path, and *in situ* 3D printing was carried out according to the planned path (Fig. 4C). The whole direct printing procedure required 12 min for completion. It should be noted that the angle and position of the printing objective should be adjusted based on the relative positions of the 3D printer and the defect. After 3D bio-printing completion, porous structures could be found in the scaffold (Fig. 4D).

Osteogenic effects

We then evaluated recovery in pigs at 12 weeks after surgery. The gross view and X-ray results are shown in Fig. S7. According to micro-CT scans at 12 weeks (Fig. 5A), restoration was more overt in the 3DP group. Gaps and cavities were clearly observed in the defect region after 3 months in the control group. In the 3DP group, a continuous cortical bone structure was found in the defect region. 3D reconstruction exhibited this phenomenon more clearly. Indeed, the blank control group (Fig. 5B) showed rough cortical bone surface and thin cortical bone tissues after 3 months, while smooth cortical bone surface and thick cortical bone tissues were found in the 3DP group. A statistically significant difference was found in BV/TV ratio between the two groups (Fig. 5C). Specifically, the 3DP group showed a larger volume of the newly-formed bone tissue. The spatial morphology of trabeculae also confirmed the abovementioned results (Fig. 5D); the 3DP group had higher Tb.N

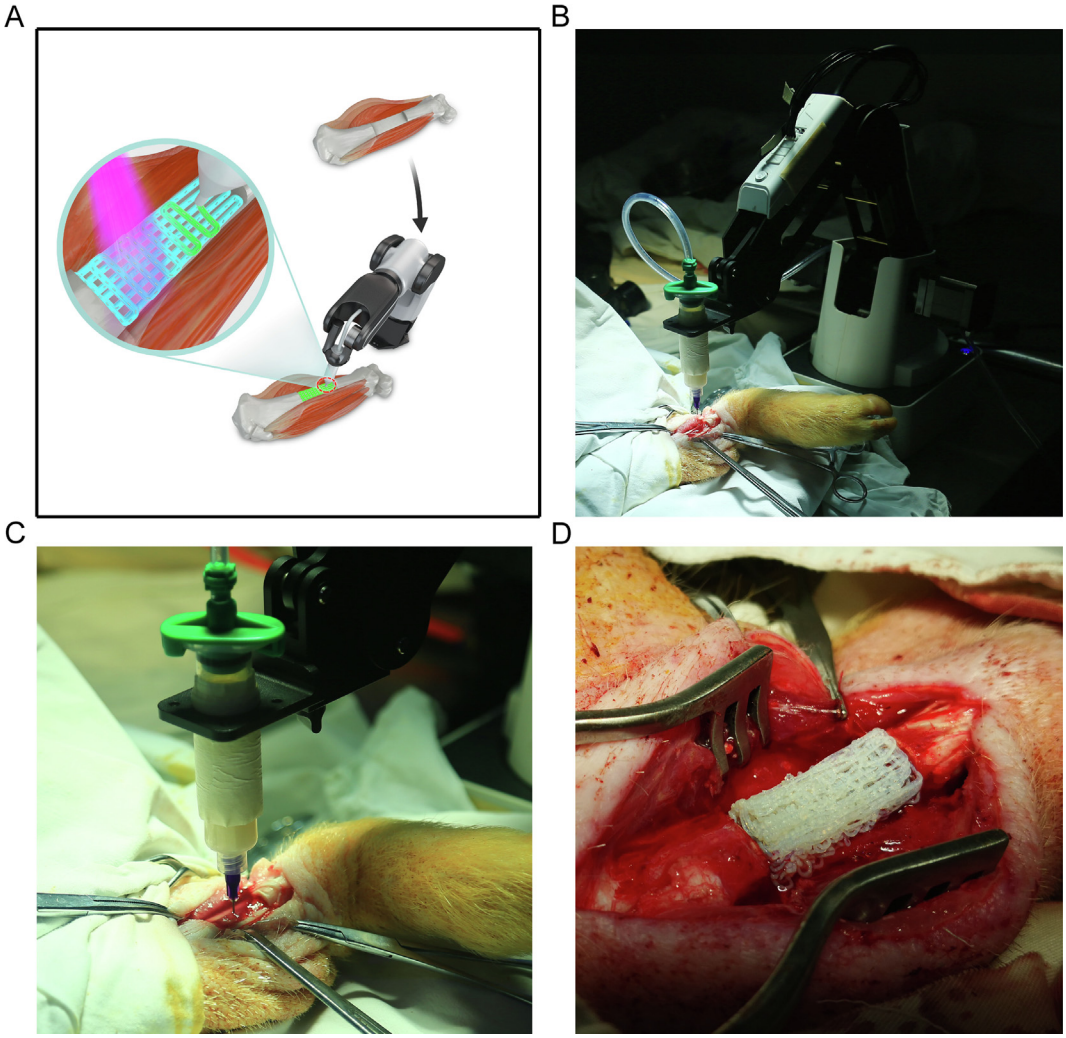

Fig. 4. Whole process of *in situ* 3D bio-printing. (A) Flow chart of the *in vivo* study. (B) General view of the robotic manipulator-based 3D printer. (C) The process of *in situ* printing. (D) Printed scaffold, with a porous structure.

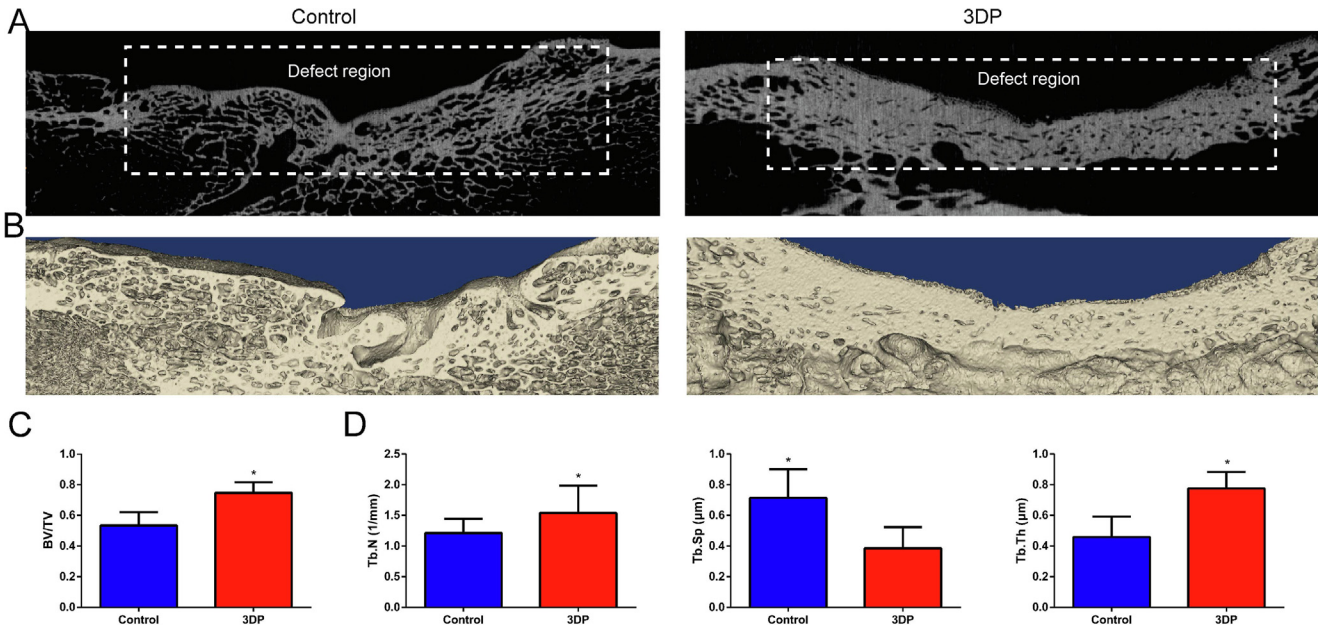

Fig. 5. *In vivo* study results. (A) Micro CT scans of the blank control and 3DP groups 12 weeks post-surgery. (B) 3D reconstruction of the blank control and 3DP groups at 12 postoperative weeks. (C) BV/TV ratios. (D) Trabecular morphology. *p < 0.05.

Table 1
Micro-CT findings.

	Control group	3DP group
BV/TV (%)	0.5347 ± 0.0879	0.7480 ± 0.1251
Tb.N (1/mm)	1.2139 ± 0.2303	1.5387 ± 0.4477
Tb.Th (μm)	0.4589 ± 0.1332	0.7757 ± 0.1091
Tb.Sp (μm)	0.7148 ± 0.1863	0.3866 ± 0.1363

and Tb.Th, and lower Tb.Sp, implying that the bone tissue in the 3DP group had improved structure and mechanical strength, and more active osteogenesis. The numerical values of the abovementioned parameters are shown in Table 1.

Histologically, Goldner trichrome (with blue-green representing the bony tissue) and H&E stained sections (Fig. S8) were assessed. In the control group (Fig. 6A–C), large cavities appeared in the newly formed bone tissue, and a disordered morphology was found. In addition, several small defects were observed on the periosteal surface. The 3DP group exhibited an improved morphology of the newly-formed bone tissue in the periosteal and mesosteal zones, with continuous periosteal surface (Fig. 6D–F). Osteoblasts were arranged regularly and compactly in these areas in the 3DP group. The histological scores for the control and 3DP groups were 10.37 ± 0.52 and 16.88 ± 0.95, respectively.

Discussion

The present study firstly presented a robotic manipulator controlled extrusion-based layer-by-layer construction of a photopolymerization bio-ink with favorable therapeutic effects on long segmental bone defects in a large animal model. This was a systematic study that integrated material science, engineering technology and clinical medicine. Use of the *in situ* 3D bioprinting technology for direct injury repair faces enormous challenges, with a huge gap between basic research and clinical application, including 1) the synthesis of biomaterials, 2) formation of scaffolds with defect-like shapes, and 3) development of an appropriate 3D bio-printer. Among these challenges, fast and biocompatible crosslinking of the bio-ink is the foundation of *in situ* 3D printing. The commonly used crosslinking methods that require

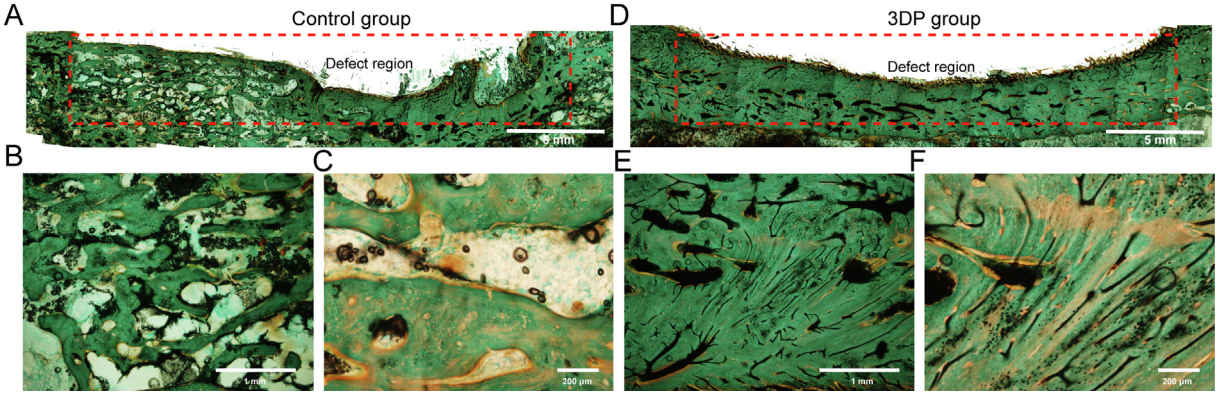

Fig. 6. Goldner trichrome results. (A) General view of the injured region in the blank control group. Goldner trichrome stained sections analyzed at 40x (B) and 100x (C) in the control group. (D) General view of the injured region in the 3DP group. Goldner trichrome stained samples assessed at 40x (E) and 100x (F) in the 3DP group.

high temperature and non-physiological ionic concentrations are obviously not suitable for *in vivo* bio-printing [25,26]. Reactions that are too slow or generate undesirable side products should also be avoided. Moreover, the physiological environment is filled with body fluids, which may exert negative effects on bio-ink gelation and yield unfavorable printing shapes. Reducing the reaction time with mild reaction conditions *in situ* is vital for the realization of precision printing structures. Another crucial factor is the 3D bio-printer, which represents the direct executor of *in situ* bio-printing. Traditional 3D printers usually consist of a ball-screw drive system, and are large and heavy. The printing space is limited by the length of the ball-screw system, reducing convenience and maneuverability in direct 3D printing for tissue repair. A 3D bio-printer with a smaller volume and a larger working space is the future target in developing this type of instrument.

To achieve direct 3D bio-printing, two aspects must be considered consecutively. The first is to select a suitable 3D printing technique for the target tissue. For instance, inkjet bio-printing is appropriate for skin wound repair because the damaged area is superficial and generally large [27]. Compared with other techniques, inkjet bio-printing results in faster and more complete wound coverage although its molding ability is weak. However, for bone and cartilage remolding, extrusion-based techniques are more appropriate [14–16]. This additive manufacturing technology has a strong capability of constructing scaffolds with specific shapes. Compared with soft tissue repair, bone and cartilage restoration is more likely affected by mechanical strength, shape, and pore structure [28]. Therefore, we selected the extrusion-based printing method to complete the repair process. The diameter of the printing nozzle could be adjusted according to the injured area and bio-ink viscosity. Based on our previous studies, a nozzle diameter ranging from 180 μm to 400 μm is optimal for cartilage and bone repair [14,20]. Filaments of this diameter range achieve suitable pore size and macroscopic shape in an acceptable time frame. In presence of light, printing accuracy increases notably, and photopolymerization can stimulate the cross-linking of bio-ink filaments in a few seconds and maintain optimal porous characteristics (pore size, porosity, and distribution) of the digital model [20,29]. Besides appropriate 3D printing parameters, the 3D printer itself is a critical factor in *in situ* 3D printing. In order to overcome the limited working space and the giant spatial volume, the 4-DOF robot was applied in place of the traditional 3D printer. Nevertheless, robots are generally designed for industrial utilization, and absolute positioning accuracy is very poor due to differences between the kinematics model used by the robot controller and the actual kinematics [30]. The printing accuracy of robots is restricted because of potential errors. Through calibration, the kinematic accuracy of the robot reached 0.5 mm in this study, which was much higher than that of the robot-assisted dynamically referenced system (>1 mm), indicating that the modified 4-DOF robot could fully satisfy the physical requirements of clinical orthopedic treatment [31]. Compared with the traditional three-axis motion system, the robot provided a larger operation space with a smaller instrumentation volume. Moreover, the robot could produce the customized shape at the injured region directly, avoiding the risk of contamination. This advantage reflects the potential of the new 3D printing modality for clinical application, e.g., in non-contact diagnosis and treatment. During pandemics, including novel coronavirus infection (COVID-19), plague, Middle East Respiratory Syndrome (MERS), and Ebola virus infection, non-contact diagnosis and treatment methods using robots can reduce the risk of infection and transmission, and better protect the medical staff and patients.

Although kinematic accuracy was satisfactory, the printing resolution still needs improvement. As shown in the *in vivo* study, pore size and distribution in the printed structure differed from those of the planning path to a certain extent. This may be due to the effect of the body fluid and small displacement on bio-ink crosslinking and deposition, which is the second aspect to be considered in *in situ* 3D bio-printing. A suitable bio-ink for *in situ* printing should meet several requirements, including an appropriate viscosity for maintaining the shape before crosslinking, cell attachment, and cell functions of proliferation and differentiation, as well as mimicry of mechanical characteristics of the natural tissue [32]. We introduced a double-network hydrogel as bio-ink in this work. By adding GelMA, bio-ink's viscosity increased and was more suitable for 3D printing. However, the extruded bio-ink might stick to the nozzle tip, resulting in viscous imprint volume drag or infill deformation [15]. This led to material deposition outside the printing area and reduced printing accuracy. This was the major reason for the error occurring in the current *in vivo* study. Apart from viscosity, mechanical strength is also momentous in bone repair. For the bio-ink in this study, alginate chains were cross-linked by calcium (Ca^{2+}), and PEGDA and GelMA formed a polymeric network through covalent cross-linking. Alginate hydrogels have been shown to promote bone formation *in vitro* and *in vivo* [33]. The combination of alginate, PEGDA and GelMA led to a suitable degradation rate and stronger mechanical properties [34,35]. This unique double network structure ensures the stretchability of the bio-ink and provides sufficient strength and stiffness until bone remolding. This was demonstrated by the above mechanical tests. The strain stiffening behavior of the hydrogel plays a critical role in load bearing during damage repair. The fast recovery capability also benefits bone restoration, since mechanical properties can be recovered quickly after load release. A bio-ink with such characteristics can resist deformation by the hydrogel *in vivo* to some extent and maintain the ability of transmitting stress, which plays a vital role in bone remolding.

To maintain the shape before the photo-crosslinking reaction, we increased the viscosity of the bio-ink instead of adding cells due to the low cell viability reported in high viscosity microenvironments [36]. However, addition of GelMA not only benefited the mechanical strength, but also increased biocompatibility, preserving high cell viability. Multiple studies have demonstrated that the hydrogel enhances osteogenetic ability [37]. Owing to the massive amount of bone marrow stromal cells (BMSC) from the marrow cavity, the arginine-glycine-aspartic acid (RGD) sequences in GelMA can promote cell attachment *in situ* [38]. Moreover, matrix metalloproteinase (MMP) target sequences also accelerate tissue repair. In addition to biological advantages, the mechanical properties of GelMA also play a vital role in guaranteeing favorable treatment effects in the 3DP group. Reaction onset time, reaction rate, and biocompatibility could be adjusted by altering light intensity in this mechanical tunable hydrogel. According to previous findings, a light intensity of 150 mW/cm^2 preserves high cell viability with a short reaction onset time (<10 s), while the crosslinking rate increases rapidly during the early stage of the reaction [39]. Accordingly, the hybrid bio-ink used in this study represents a promising guided bone regeneration material. The above *in vivo* study demonstrated that the defect volume could be restored by more than 70% in 12 weeks without cells or growth factors detected in the bio-ink, indicating the potential therapeutic advantage in case suitable drugs or growth factors are added to the bio-ink. This also provided a further research direction, since an ideal biomaterial structure with appropriate drug-delivery systems, such as polylactic-co-glycolic acid (PLGA) nanoparticles, polydopamine, and bone morphogenetic protein 2 (BMP-2), may improve the osteogenic potential [40,41].

Compared with previous implantation outcomes, bone repair in this study was acceptable, and the operative time was significantly decreased [42,43]. The reduced time can be beneficial as the patient does not have to be under anesthesia for long. More impor-

tantly, the *in situ* bio-printing technology can decrease surgeon dependency, ease scaffold handling and reduce non-sterile exposure of the scaffolds. In clinical treatment for bone healing, the vascularized bone graft has been considered the gold standard in the past four decades [44]. However, patients must undergo lengthy operations in case of massive bone defects because of the limited volume in donor sites, including the iliac crest, ribs, and fibula. Unlike the traditional therapeutic method, the *in situ* 3D bio-printing technology can save weeks of preoperative preparation, resulting in early rehabilitation and less complications postoperatively. This superiority is another great advantage of this technology, which should be further developed for clinical application.

Compliance with Ethics Requirements

All Institutional and National Guidelines for the care and use of animals (fisheries) were followed.

Declaration of Competing Interest

The authors declare that they have no known competing financial interests or personal relationships that could have appeared to influence the work reported in this paper.

Acknowledgments

General: We would like to thank Professor Hui Wei (College of Engineering and applied Sciences, Nanjing University) for valuable suggestions.

Funding

The current work was funded by the National Natural Science Foundation (NSFC 81420108021, 81730067 and 81802135), the National Key Research and Development Project (2018YFF0301101), the Key Research and Development Project of Jiangsu Province (BE2018010-3), Jiangsu Provincial Key Medical Center Foundation, and Jiangsu Provincial Medical Outstanding Talent Foundation.

Appendix A. Supplementary material

Supplementary data to this article can be found online at https://doi.org/10.1016/j.jare.2020.11.011.

References

[1] Nauth A, Mckee MD, Einhorn TA, Watson JT, Li R, Schemitsch EH. Managing bone defects. J Orthop Trauma 2011;25:462–6.
[2] Cyril M, Brian Thomas B, Wade S. Management of segmental bone defects. J Am Acad Orthop Surgeons 2015;23:143–53.
[3] Henkel J, Woodruff MA, Epari DR, Steck R, Glatt V, Dickinson IC, et al. Bone regeneration based on tissue engineering conceptions - a 21st century perspective. Bone Res 2013;1:216–48.
[4] Loeffler BJ, Kellam JF, Sims SH, Bosse MJ. Prospective observational study of donor-site morbidity following anterior iliac crest bone-grafting in orthopaedic trauma reconstruction patients. J Bone Joint Surgery-Am 2012;94A:1649–54.
[5] Seol YJ, Kang HW, Lee SJ, Atala A, Yoo JJ. Bioprinting technology and its applications. Eur J Cardio-thoracic Surgery: Off J Eur Assoc Cardio-thoracic Surg 2014;46:342–8.
[6] Lai JC, Li L, Wang DP, Zhang MH, Mo SR, Wang X, et al. A rigid and healable polymer cross-linked by weak but abundant Zn(II)-carboxylate interactions. Nat Commun 2018;9:2725.
[7] Vanderburgh JP, Fernando SJ, Merkel AR, Sterling JA, Guelcher SA. Fabrication of trabecular bone-templated tissue-engineered constructs by 3D inkjet printing. Adv Healthcare Mater 2017;6:1700369.
[8] Yang Y, Wu P, Wang Q, Wu H, Liu Y, Deng Y, et al. The enhancement of Mg corrosion resistance by alloying Mn and laser-melting. Materials 2016;9:216.
[9] Briquez PS, Hubbell JA, Martino MM. Extracellular matrix-inspired growth factor delivery systems for skin wound healing. Adv Wound Care 2015;4. 150127064149004.
[10] Badylak SF, Nerem RM. Progress in tissue engineering and regenerative medicine. PNAS 2010;107:3285–6.
[11] Mertz L. Tissue engineering and regenerative medicine: the promise, the challenges, the future. IEEE Pulse 2017;8:15.
[12] Fu Y, Xia W, Chen X. 3D printing of porous alginate/gelatin hydrogel scaffolds and their mechanical property characterization. Int J Polym Mater Polym Biomater 2016;66. 00914037.2016.1201830.
[13] Duan B, Hockaday LA, Kang KH, Butcher JT. 3D bioprinting of heterogeneous aortic valve conduits with alginate/gelatin hydrogels. J Biomed Mater Res Part A 2013;101:1255–64.
[14] Li L, Yu F, Shi J, Shen S, Teng H, Yang J, et al. In situ repair of bone and cartilage defects using 3D scanning and 3D printing. Sci Rep 2017;7:9416.
[15] Lipskas J, Deep K, Yao W. Robotic-assisted 3D bio-printing for repairing bone and cartilage defects through a minimally invasive approach. Sci Rep 2019;9:3746.
[16] Di Bella C, Duchi S, O'Connell CD, Blanchard R, Augustine C, Yue Z, et al. In situ handheld three-dimensional bioprinting for cartilage regeneration. J Tissue Eng Regener Med 2018;12:611–21.
[17] Ma K, Zhao T, Yang L, Wang P, Jin J, Teng H, et al. Application of robotic-assisted in situ 3D printing in cartilage regeneration with HAMA hydrogel: an in vivo study. J Adv Res 2020;23:123–32.
[18] Loessner D, Meinert C, Kaemmerer E, Martine LC, Yue K, Levett PA, et al. Functionalization, preparation and use of cell-laden gelatin methacryloyl-based hydrogels as modular tissue culture platforms. Nat Protoc 2016;11:727–46.
[19] Gao Q, Liu Z, Lin Z, Qiu J, Liu Y, Liu A, et al. 3D bioprinting of vessel-like structures with multilevel fluidic channels. ACS Biomater Sci Eng 2017;3:399–408.
[20] Yu F, Han X, Zhang K, Dai B, Shen S, Gao X, et al. Evaluation of a polyvinyl alcohol-alginate based hydrogel for precise 3D bioprinting. J Biomed Mater Res Part A 2018;106:2944–54.
[21] Kang LH, Armstrong PA, Lee LJ, Duan B, Kang KH, Butcher JT. Optimizing photo-encapsulation viability of heart valve cell types in 3D printable composite hydrogels. Ann Biomed Eng 2017;45:360–77.
[22] Han Z, Bhavsar M, Leppik L, Oliveira KMC, Barker JH. Histological scoring method to assess bone healing in critical size bone defect models. Tissue Eng Part C, Methods 2018;24:272–9.
[23] Bertassoni LE, Cardoso JC, Manoharan V, Cristino AL, Bhise NS, Araujo WA, et al. Direct-write bioprinting of cell-laden methacrylated gelatin hydrogels. Biofabrication 2014;6:024105.
[24] Gómez-Guillén MC, Giménez B, López-Caballero ME, Montero MP. Functional and bioactive properties of collagen and gelatin from alternative sources: a review. Food Hydrocolloids 2011;25:1813–182725.
[25] Alizadehgiashi M, Khuu N, Khabibullin A, Henry A, Tebbe M, Suzuki T, et al. Nanocolloidal hydrogel for heavy metal scavenging. ACS Nano 2018;12:8160–8.
[26] Sun W, Xue B, Li Y, Qin M, Wu J, Lu K, et al. Polymer-supramolecular polymer double-network hydrogel. Adv Funct Mater 2016;26:9044–52.
[27] Skardal A, Mack D, Kapetanovic E, Atala A, Jackson JD, Yoo J, et al. Bioprinted amniotic fluid-derived stem cells accelerate healing of large skin wounds. Stem Cells Translat Med 2012;1:792–802.
[28] Zadpoor AA. Bone tissue regeneration: the role of scaffold geometry. Biomater Sci 2015;3:231–45.
[29] Zuo Y, Liu X, Wei D, Sun J, Xiao W, Zhao H, et al. Photo-cross-linkable methacrylated gelatin and hydroxyapatite hybrid hydrogel for modularly engineering biomimetic osteon. ACS Appl Mater Interfaces 2015;7:10386.
[30] Zeng Y, Tian W, Liao W. Positional error similarity analysis for error compensation of industrial robots. Rob Comput Integr Manuf 2016;42:113–20.
[31] Dunbar NJ, Roche MW, Park BH, Branch SH, Conditt MA, Banks SA. Accuracy of dynamic tactile-guided unicompartmental knee arthroplasty. J Arthroplasty 2012;27. 803–8.e1.
[32] Diogo GS, Gaspar VM, Serra IR, Fradique R, Correia IJ. Manufacture of beta-TCP/alginate scaffolds through a Fab@home model for application in bone tissue engineering. Biofabrication 2014;6:025001.
[33] Yang J, Zhang YS, Yue K, Khademhosseini A. Cell-laden hydrogels for osteochondral and cartilage tissue engineering. Acta Biomater 2017;57:1–25.
[34] Wang Y, Ma M, Wang J, Zhang W, Lu W, Gao Y, et al. Development of a photo-crosslinking, biodegradable GelMA/PEGDA hydrogel for guided bone regeneration materials. Materials (Basel, Switzerland) 2018;11.
[35] Zehnder T, Sarker B, Boccaccini AR, Detsch R. Evaluation of an alginate-gelatine crosslinked hydrogel for bioplotting. Biofabrication 2015;7:025001.
[36] Tabriz AG, Hermida MA, Leslie NR, Shu W. Three-dimensional bioprinting of complex cell laden alginate hydrogel structures. Biofabrication 2015;7:045012.
[37] Slaughter BV, Khurshid SS, Fisher OZ, Khademhosseini A, Peppas NA. Hydrogels in regenerative medicine. Adv Mater 2010;21:3307–29.
[38] Yunxiao L, Chan-Park MB. A biomimetic hydrogel based on methacrylated dextran-graft-lysine and gelatin for 3D smooth muscle cell culture. Biomaterials 2010;31:1158–70.

[39] OConnell CD, Zhang B, Onofrillo C, Duchi S, Blanchard R, Quigley A, et al. Tailoring the mechanical properties of gelatin methacryloyl hydrogels through manipulation of the photocrosslinking conditions. Soft Matter 2018;14:2142–51.
[40] Bjorkenheim R, Stromberg G, Ainola M, Uppstu P, Aalto-Setala L, Hupa L, et al. Bone morphogenic protein expression and bone formation are induced by bioactive glass S53P4 scaffolds in vivo. J Biomed Mater Res B Appl Biomater 2019;107:847–57.
[41] Boda SK, Almoshari Y, Wang H, Wang X, Reinhardt RA, Duan B, et al. Mineralized nanofiber segments coupled with calcium-binding BMP-2 peptides for alveolar bone regeneration. Acta Biomater 2019;85:282–93.
[42] Panyu Z, Yan X, Xiaosong C, Panfeng W, Yang X, Shuogui X. Enhanced bone tissue regeneration by antibacterial and osteoinductive silica-HACC-zein composite scaffolds loaded with rhBMP-2. Biomaterials 2014;35:10033–45.
[43] Inzana JA, Diana O, Fuller SM, Kelly JP, Graeve OA, Schwarz EM, et al. 3D printing of composite calcium phosphate and collagen scaffolds for bone regeneration. Biomaterials 2014;35:4026–34.
[44] Lasanianos NG. Current management of long bone large segmental defects. Orthopaedics & Trauma 2010;24:149–63.